

Article

Pt Effect on H₂ Kinetics Sorption in Mn Oxide-Based Polymeric Material

Rolando Pedicini^{1,*}  and Michalis Sigalas²¹ CNR-ITAE, Institute for Advanced Energy Technologies, Via S. Lucia sopra Contesse 5, 98126 Messina, Italy² Department of Materials Science, University of Patras, 26500 Patras, Greece; sigalas@upatras.gr

* Correspondence: rolando.pedicini@cnr.it; Tel.: +39-090-624254

Abstract: Recent studies have demonstrated how a material based on Mn oxide, supported by a polymeric matrix, shows an interesting H₂ absorption capacity in non-drastring temperature and pressure conditions even if the reaction kinetics are particularly slow. In this study, therefore, two different percentages of Pt (5 and 10 wt%) were added to a composite sample, containing 50 wt% of Mn oxide, through a ball milling technique in order to verify the reduction in absorption kinetics of the quantity of added catalyst. The effect of the catalyst quantity on the composite matrix was investigated through morphological analyses of the SEM-EDX and TEM types, with which it was found that the distribution of Pt is more homogeneous compared to the sample containing 5%. XRD studies confirmed the simultaneous presence of the amorphous structure of the polymer and the crystalline structure of Pt, and absorption tests with the Sievert method verified a better kinetic reaction of the 10% Pt sample. In parallel, a modeling study, using the ab initio Density Functional Theory (DFT), was performed. The supercell for this study was Mn₂₂Pt₂O₄₈. The number of H atoms gradually increased, starting from 2 (Mn₂₂Pt₂O₄₈H₂), where the initial desorption energy was 301 kJ/mol, to 211 kJ/mol for 12 H atoms (Mn₂₂Pt₂O₄₈H₁₂). From the experimental H₂ absorption value (0.22 wt%), the number of respective H atoms was calculated (n = 5), and the corresponding desorption energy was equal to about 273 kJ/mol.

Keywords: composite material containing Pt; chemical–physical characterizations; hydrogen storage measurements; density functional theory calculations



Citation: Pedicini, R.; Sigalas, M. Pt Effect on H₂ Kinetics Sorption in Mn Oxide-Based Polymeric Material. *Hydrogen* **2024**, *5*, 1–13. <https://doi.org/10.3390/hydrogen5010001>

Academic Editor: George E. Marnellos

Received: 13 November 2023

Revised: 7 December 2023

Accepted: 29 December 2023

Published: 4 January 2024



Copyright: © 2024 by the authors. Licensee MDPI, Basel, Switzerland. This article is an open access article distributed under the terms and conditions of the Creative Commons Attribution (CC BY) license (<https://creativecommons.org/licenses/by/4.0/>).

1. Introduction

The transition from the use of fossil fuels to ecological energy vectors sees some very significant challenges that must be faced, and concrete answers must be given in the coming years so that the energy transition is feasible. In the case of hydrogen, one aspect to take into consideration is that of an infrastructural nature, which is linked to the transport and storage of hydrogen itself [1]. Hydrogen is both a clean energy source and an energy carrier for storage [2]. It is an energy carrier since it is a fuel for fuel cells and electrochemical devices that convert the energy produced by a chemical reaction into electrical energy. The development of fuel cells has now reached full technological maturity; however, researchers continue to study the possibility of improving the individual components, membranes [3], electrodes [4], and catalysts [5] using a qualitative approach while also trying to reduce costs.

Hydrogen storage therefore constitutes an important and critical aspect because it is at the center of the energy cycle; if unresolved, it would block the path towards the development and commercial penetration of the entire supply chain [6]. Hydrogen can be stored in large quantities for long periods; the energy produced is not lost over time and can be stored on an industrial scale and recovered as a backup energy source when needed. For example, in processes requiring high temperatures, such as those adopted by the steel industry, refineries, or fertilizer production, stored hydrogen can be used as a feedstock

for industrial applications [7]. Furthermore, hydrogen can be transported through existing gas pipelines mixed with natural gas, and in the future, with the investments envisaged by the European strategic plan, dedicated pipelines are expected to be built [8]. In the uses just mentioned, an important factor to highlight is that in all phases of production and storage, hydrogen does not generate CO₂ emissions nor other forms of emissions that are harmful to humans or pollute the environment. Hydrogen can currently be stored as a highly compressed gas [9], as a liquid at atmospheric pressure and a temperature of −253 °C [10], or in the form of solid metal hydrides [11].

The latter route is the most promising for the future, given the significant storage capacity and the intrinsic safety determined by the absence of high pressures or low temperatures. From a strategic point of view, for energy production, efforts and resources must appropriately focus on the storage and transport of solid-state hydrogen, mainly through the development of new storage materials. Unfortunately, currently, the characteristics of these compounds in the solid state require a lot of basic research to make them compatible with the requirements of commercial applications, including high gravimetric and volumetric densities, accessible working temperatures, rapid kinetics during hydrogenation/dehydrogenation processes, and resistance to decay and contamination associated with continued use cycles. Today, the greatest technological challenge to be solved for the creation of a hydrogen-based economy is represented by the identification of a material that simultaneously satisfies all of the requirements listed above.

The US Department of Energy (DoE) [12] has set some storage density conditions that should be achieved by 2025, which are 0.055 kg of H₂ per kg of the system in a solid state and 0.040 kg of H₂ per liter in liquid form. The materials that are suitable for the accumulation of hydrogen in the solid state, on which international research is focusing, essentially belong to two different classes [13]. These classes can be distinguished by the different types of bonds they form with hydrogen; physisorption [14] occurs through weak Van der Waals surface bonds exploiting the morphological characteristics of the materials, and chemisorption occurs through strong covalent bonds [15]. The first class includes all carbonaceous materials, such as nanotubes [16], activated carbons [17,18], fullerenes [19], graphenes [20], and MOFs [21], whose main characteristics are to possess a high surface area (over 2000 m²/g) and to have good adsorption capacity, even above 6 wt%, but only in low T conditions (−196.15 °C). This last condition undoubtedly limits its use on a large scale, especially for mobile applications, and also overlaps with the liquid hydrogen technique that is already used in cars, which shows the unsolved problems of hydrogen boil-off [22].

Among the materials belonging to the second class, there are metal hydrides and composite materials. Metal hydrides can be divided into interstitial [23] and complex [24] classes. In the first class, hydrogen enters a solid solution in metal crystals in the atomic or ionic state and can be extracted “almost” irreversibly. This class includes Mg alloys (for example, Mg-Ni) [25], rare earth alloys (La-Ni and others) [26], and ternary and quaternary transition metal alloys (such as Ti-Cr-Mo and Zr-Ti-V-Ni) [27]. In the second class of materials, hydrogen is chemically bonded. Since the extraction of hydrogen from the compound implies its decomposition, the search for recovery procedures for the degradation products is of fundamental importance from an economic and ecological point of view. This class includes alanates (NaAlH₄, LiAlH₄, etc.) [28], which have an average accumulation capacity of the order of 5 wt%; amides (LiNH₂) and imides (Li₂NH) [29,30], which accumulate approximately 7 wt%; and borohydrides (NaBH₄ and LiBH₄), which accumulate approximately 11 wt% [31].

Over the years, many composite materials have been investigated in more or less drastic T and P conditions. The reversibility of the charge/discharge cycles is a critical and fundamental aspect. The materials used for storage are subjected to strong mechanical stresses, which cause the collapse of the structures and the consequent loss of reversibility. For this reason, some studies have directed their attention towards polymer composite materials, even if only a few articles have been published on the use of synthetic polymers

in this specific application. The mechanical properties of polymers attenuate the structural stress that occurs during the abs/des cycles that the material can undergo. A possible explanation for this could be the interaction between hydrogen and polymer chains and/or metal hydrides supported on these polymers. These interactions are generally a combination of covalent, ionic, metallic, H-bonds, and van der Waals bonds [32]. These polymeric materials, compared to commercial metal hydrides, could be used due to their lightness, cheapness, and non-reactivity in air, especially for portable and automotive applications. Other important aspects that make these materials quite interesting are their low density and low costs (the syntheses are easy to create). Some transition metal oxides, such as TiO_2 and manganese (IV) oxide, MnO_2 , have been tested as dopants to improve the H_2 absorption properties of light metals [33] and complex hydrides [34] and could also play a positive role in the interaction of hydrogen with the polymer matrix. In the wake of these results, an alternative path was undertaken with interesting results [35–37], which produced a demonstration laboratory cylinder of approximately 20 L containing the synthesized material [38]. The problem with this type of material lies in the kinetics of the H_2 absorption reaction being too slow.

In this work, two percentages of Pt-based catalysts (5 and 10 wt%) were selected and added to a polymer matrix containing 50 wt% Mn oxide. A complete series of chemical–physical characterizations has allowed us to demonstrate how the higher percentage of Pt produces an improvement in the H_2 absorption kinetics.

2. Materials and Methods

2.1. Composite Materials Synthesis

The first phase of the synthesis of the composite material involved the chlorosulfonation of commercial Polyetheretherketone (PEEK) (Victrex, Guzman Polymers Srl distributor, Castelfranco Veneto, Treviso, Italy) through the use of chlorosulfonic acid at 30 °C for 24 h. The 100% chlorosulfonated polymer was subsequently treated with 0.1 M of KMnO_4 solution under the same conditions as previously reported [35]. A percentage of 50 wt% of Mn oxide was verified through ashes analysis; it was carried out using a muffle, burning a small portion of the sample at 1000 °C.

Two different platinum catalyst (Alfa Aesar-Pt black, distributor Thermo Fischer Scientific™, Waltham, MA, USA) weight percentages were mixed, 5 and 10 wt%, respectively, into a composite material through a ball milling technique (model Fritsch Pulverisette 6, EMME3 srl distributor, Lainate, Milano, Italy). The reaction jar and the five spheres were made of stainless steel (Fritsch, EMME3 srl distributor, Lainate, Milano, Italy). Some synthesis parameters were paid attention to and selected, such as sphere/powder ratio (10/1), rotation speed (300 rpm), and mixing time (3 h).

2.2. SEM-EDX and TEM Analyses

A field emission scanning electron microscope (SEM) equipped with an EDAX microprobe (Philips model XL30 S FEG) was used to study both the morphology and the qualitative analyses of the powders. All of the samples were fixed on the adhesive stab, successively, to make them electrically active, and a graphite cover was performed. In this study, different magnifications operating at an accelerating voltage of 20 kV were used.

EDX mapping on the powders was performed by using a field emission scanning electron microscope equipped with an EDAX microprobe. Pt, Mn, S, Cl, and K were mapped by utilizing L and K lines. The mapped surface was about $20 \mu\text{m} \times 10 \mu\text{m}$, and the used mapping matrix had dimensions of 256×200 .

2.3. X-ray Diffractions

X-ray powder diffraction (XRD) analysis was performed on powders, both synthesized materials and commercial platinum, using a Philips X-ray automated diffractometer (model PW3710) with a Cu-K α radiation source. The 2θ Bragg angles were scanned between 5 and 100 2θ .

2.4. Pressure Composition Isotherm Tests

The PCT Pro 2000 gas sorption analyzer (SETARAM Instrumentation, Automation seller, Abbiategrasso, Milano, Italy) is an automated instrument that allows for the estimation of the quantity of hydrogen absorbed or released by the materials under examination. With the PCT Pro 2000, it was possible to carry out various types of tests for the characterization of materials; kinetic tests were performed to investigate the kinetics of hydrogen absorption processes at a fixed initial temperature and pressure. These tests play fundamental roles in studying the effect of Pt on the hydrogen absorption reaction kinetics. From the tests performed and reported in previous works [37], a temperature of 110 °C was chosen with a pressure range from 5 to 20 bar. Before each measurement, a vacuum-drying treatment was performed directly in the volumetric measurement chamber for approximately 24 h.

2.5. Density Functional Theory (DFT) Calculations

Calculations based on the density functional theory were performed. As in our previous study [37], a supercell of 2 by 2 by 3 MnO₂ unit cells (containing 24 Mn and 48 O) was used. Two of the Mn atoms were replaced with Pt. Then, hydrogen atoms were placed inside the supercell, and the geometry of the structure was optimized. In each case, several different locations of H were obtained and optimized to find the one with the lowest energy. The desorption energy is given by Equation (1):

$$\Delta E = (E(\text{Mn}_{22}\text{Pt}_2\text{O}_{48}) + n/2 E(\text{H}_2) - E(\text{Mn}_{22}\text{Pt}_2\text{O}_{48}\text{H}_n))/n \quad (1)$$

where $E(\text{Mn}_{22}\text{Pt}_2\text{O}_{48})$, $E(\text{Mn}_{22}\text{Pt}_2\text{O}_{48}\text{H}_n)$, and $E(\text{H}_2)$ are the calculated total energies.

3. Results

In order to check the reproducibility of the base material and to verify the XRD patterns of the two catalyzed samples, X-ray analyses were carried out. As can be seen in Figure 1a, the SPMnO sample with 50% wt of MnO₂ reproduces the same result as previously obtained [36]. The X-ray characterizations have shown that, despite the mixing between the catalyst and the polymer, the crystalline structure of Pt remains unchanged, maintaining the typical properties of the parent metal.

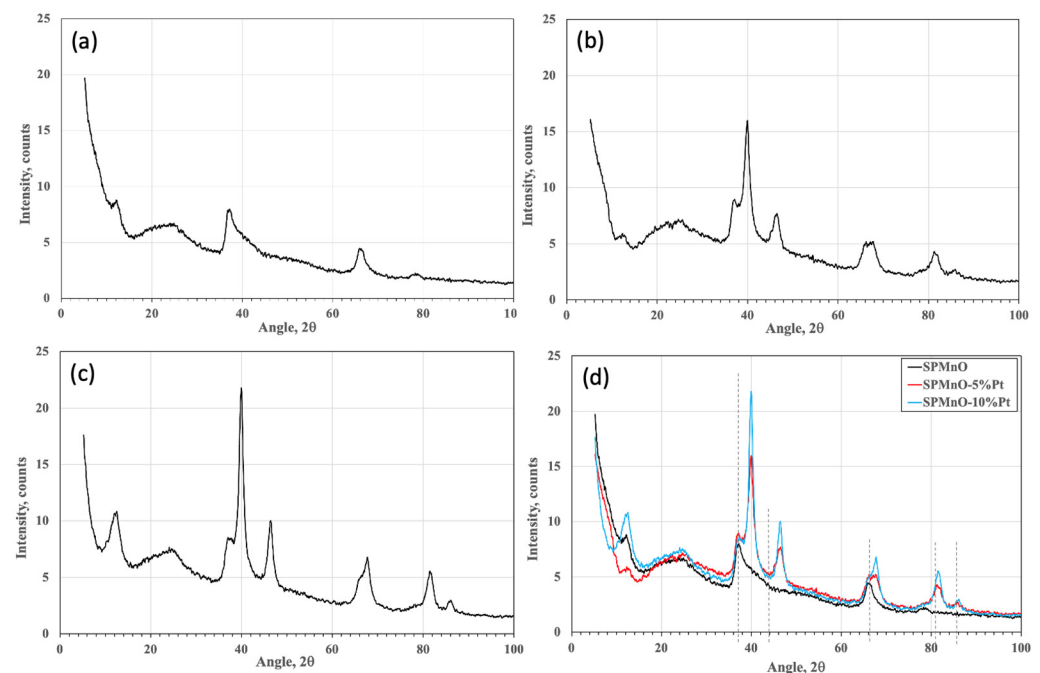


Figure 1. (a) SPMnO, (b) SPMnO-5%Pt, (c) SPMnO-10%Pt, and (d) comparison among all samples.

Figure 1b,c show how, as the percentage of Pt increases, the crystalline peaks of the metal, shown in Figure 1d, are more evident. From the comparison of Figure 1d, it is evident that there is a perfect overlap between the amorphous structure of the polymer and the crystalline structure of Pt [39]. The three characteristic peaks of Birnessite (mixed oxide based on MnO_2) positioned at 12° , 37° , and 66° 2θ are distinguished from the characteristic peaks of the Pt positioned at 39.6° , 47.4° , 67.1° , 81.2° , and 83.6° 2θ , corresponding to the reflection planes (111), (200), (220), (311), and (222), and representing a face-centered cubic crystal structure (JCPDS Card 04-0802). This indicates how, although mixing with the composite polymer has taken place, the crystalline structure of Pt remains unaltered, maintaining the typical characteristics of the starting metal [40].

To verify the morphology of the synthesized samples, SEM analyses were performed, and on the catalyzed samples, EDX mapping was carried out to verify their arrangement in the polymer matrix, and a semi-quantitative evaluation was made. The globular morphology of the polymer containing Mn oxide is shown in Figure 2e, where the homogeneity of the structure is quite evident.

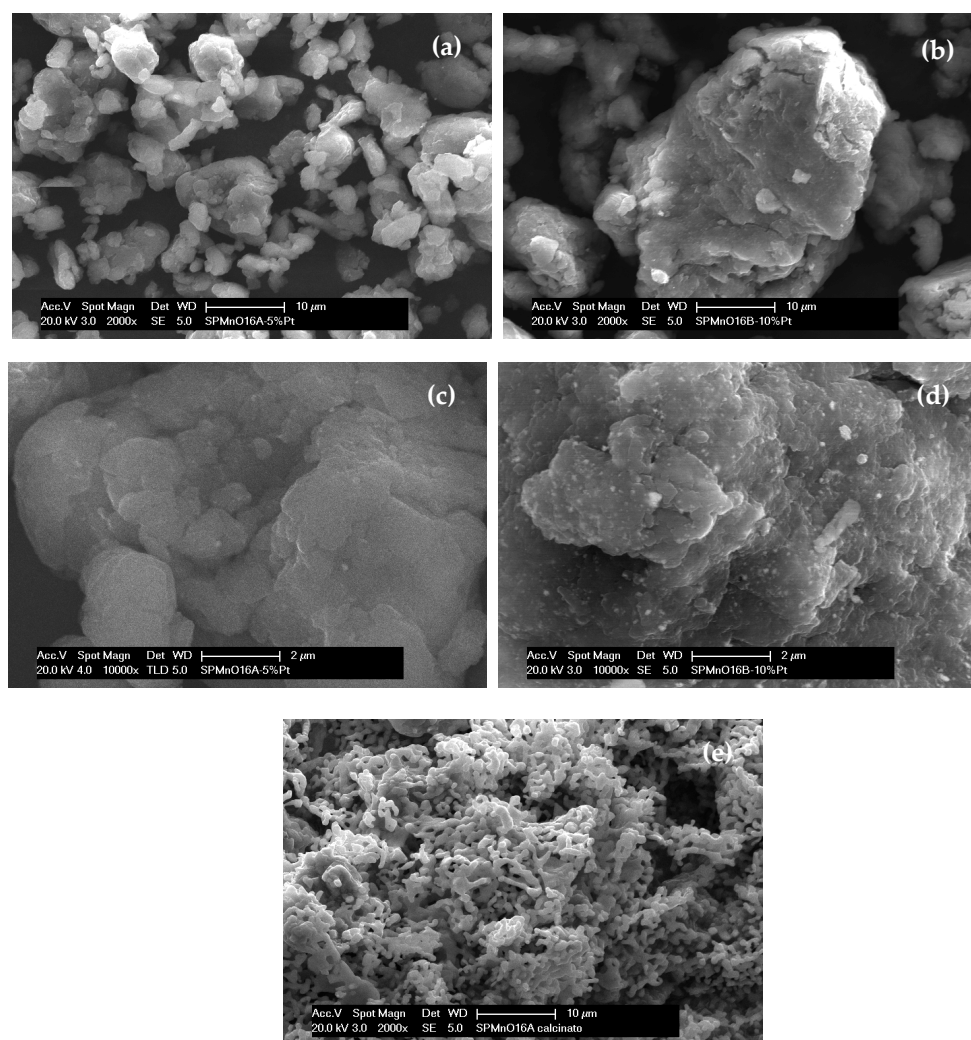


Figure 2. SEM images related to (a,c) SPMnO-5%Pt, (b,d) SPMnO-10%Pt, and (e) SPMnO.

By comparing the catalyzed samples with each other, it is clear that there is a difference in terms of the morphology at magnifications that are not too high ($2000\times$) (Figure 2a,b); the 5%Pt sample, compared to the 10%Pt sample, shows a more similar appearance with the base polymer (Figure 2e), while 10%Pt shows a denser and more compact structure. At higher magnifications ($10,000\times$) (Figure 2c,d), it can be seen how the arrangement of the Pt

on the polymer surface is more homogeneous for the 10%Pt sample compared to the 5%Pt sample, even if in the former one, some Pt agglomerates can be seen, which could suggest an incomplete mixing time.

EDX mapping, as can be seen from Figure 3, confirmed that there a greater homogeneity of the Pt for the 10%Pt sample compared to the 5%Pt sample, which was seen in the SEM images. The data reported are the results of an average of over five areas studied, and the semi-quantitative analyses confirm the real percentages of Pt in the two samples, where the Pt/Mn ratios are 0.053 (~5%Pt) and 0.11 (~10%Pt), respectively, which are very similar to the theoretical values.

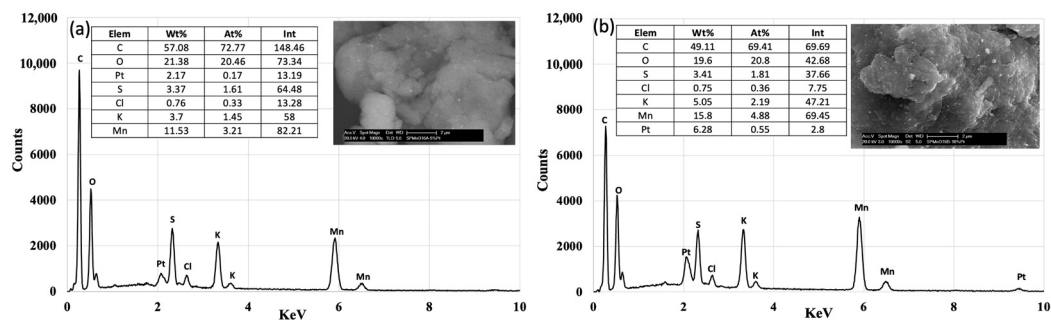


Figure 3. EDX mapping of SPMnO-5%Pt (a) and SPMnO-10%Pt (b) with relative percentages in the tables.

A further confirmation of the greater presence and homogeneous arrangement of Pt in the studied area was obtained from the TEM analyses (Figure 4), from which it can be seen how the Pt is more uniformly distributed for the 10%Pt (b) sample compared to the 5%Pt sample (a). However, as hypothesized with the preliminary SEM analyses, the greater presence of nanoparticle Pt with agglomerates of around 100 nm demonstrates how a greater mixing time is probably necessary to further homogenize the dimensions of the catalyst.

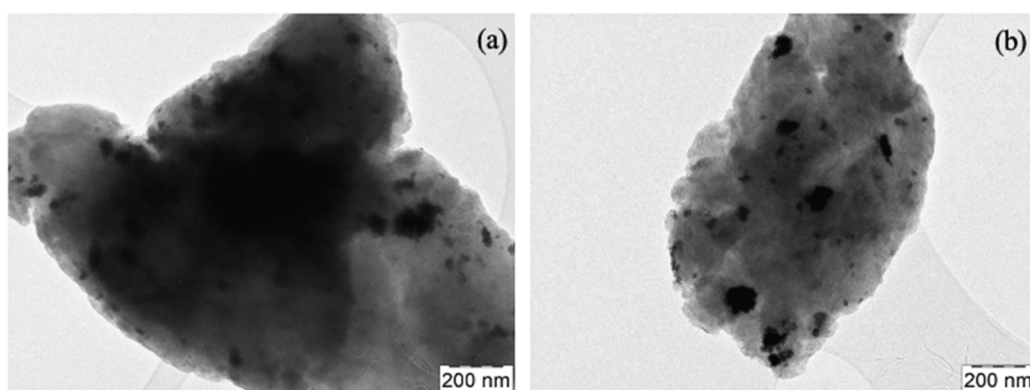


Figure 4. (a) SPMnO-5%Pt and (b) SPMnO-10Pt TEM images.

Through the use of Sievert-type volumetric equipment, the hydrogen absorption capacities of the synthesized samples and the related kinetics were verified in the conditions of $T = 110\text{ }^{\circ}\text{C}$ and P steps from 5 to 20 bars.

The established reaction time was 60 h for all of the analyzed samples. The H_2 sorption tests relating to the base sample, SPMnO-50% (Figure 5a), demonstrate how the overall storage capacity is very low (0.08 wt%), and the kinetics are homogeneously low, up to 20 bar. As can be seen from Figure 5b, no absorption-related support is provided by Pt, characterized under the same operative conditions. The addition of 5% of catalyst, as shown in Figure 5c, results in a very slight effect on the total absorption capacity (about

0.1 wt%), but from the pressure steps, an acceleration phase of the reaction can be seen at 5 bar, while at 10 and 20 bar, the slopes remain similar to the reference sample.

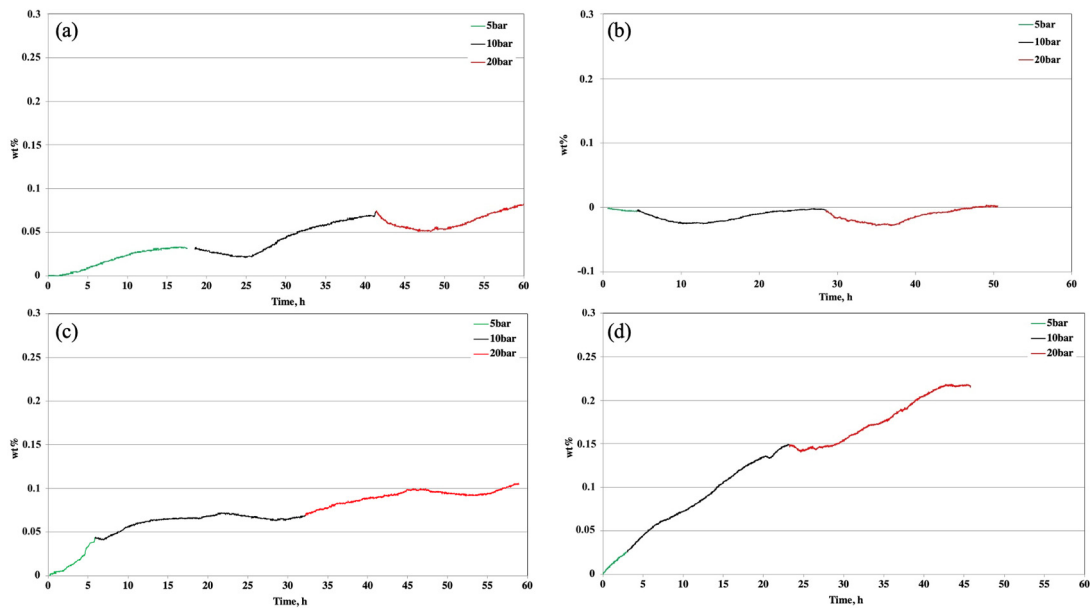


Figure 5. H₂ sorption test related to (a) SPMnO, (b) commercial Pt, (c) SPMnO-5%Pt, and (d) SPMnO-15%Pt.

The real contribution of Pt is evident when its percentage increases to 10% (Figure 5d); it is noted that after 50 h, the absorption doubles (over than 0.2 wt%), and the reaction kinetics at all pressures show a higher velocity if compared to the kinetics of the other samples. It can be assumed that the percentage of 5% Pt is not sufficient to catalyze the sorption reaction, even if the pressure is increased above 5 bar, contrary to what happens with a metal load of 10% in which a homogeneity of speed increases in all pressure steps.

It is observed that with the increase in pressure, the hydrogen adsorption in SPMnO is enhanced due to the hydrogen physisorption phenomenon. In the catalyzed materials, hydrogen sorption was achieved by two simultaneous mechanisms: physisorption and chemisorption.

To verify the degree of variation in the kinetics of the absorption reaction, Figure 6 shows the hydrogen absorption variation as a function of time. The change in P between the beginning and the end of each phase is related to the time required for reach equilibrium at each pressure.

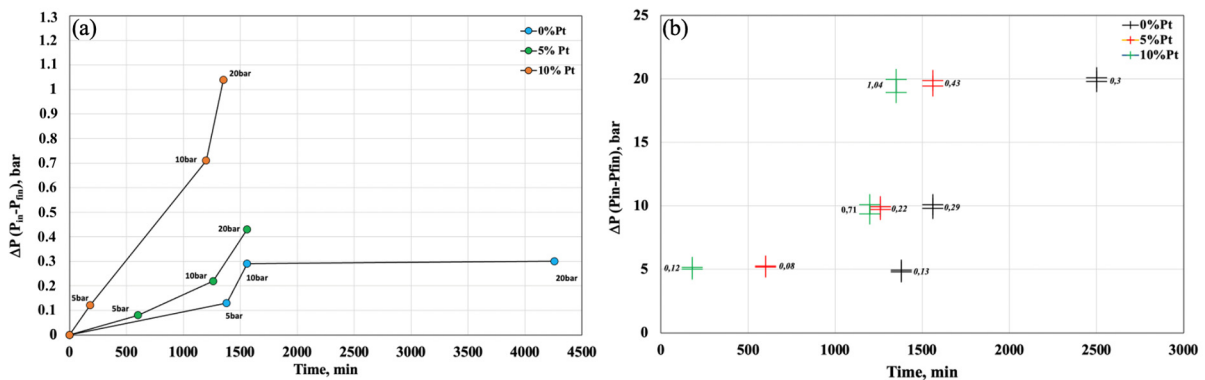


Figure 6. H₂ sorption variation trend qualitative (a) and quantitative (b).

The degree of slope of the half-line provides information on the speed of the reaction; in fact, between one pressure step and the next, the slope of the half-line is more pronounced

for the sample with 10% Pt than for the other two samples. A more evident phenomenon occurs when considering the step between 10 and 20 bar, where the slope of the half-line is much steeper, indicating that the reaction is faster than in the other two samples, and the opposite figure also shows the differences in P between the beginning and the end of the step, whose value Δ is 1.04, which is the highest value when compared to the others.

With the experimental data obtained, a calculation was performed to determine the difference in terms of the volumetric hydrogen storage capacity in the synthesized samples, as reported in Table 1, by following the formula below:

$$[\text{H}_2 \text{ mass/sample volume}] = [\text{H}_2 \text{ mass/sample mass}] \times \text{sample density} \quad (2)$$

Table 1. H₂ volumetric capacity values for synthesized materials.

Sample	Mass, g	Density, g dm ⁻³	Volume, dm ³	Exp H ₂ , wt%	H ₂ Mass, g	H ₂ Volumetric Capacity, g dm ³
SPMnO50%	0.5245	317.2	0.00165	0.08	0.0004	0.2545
SPMnO-5%Pt	0.5941	529.6	0.0011	0.1	0.0006	0.5363
SPMnO-10%Pt	0.5449	820.6	0.00066	0.22	0.0012	1.81

As can be seen from the data obtained, the 10 wt% contribution of Pt becomes important not only because of the improvement in reaction kinetics but also because it induces a noticeable improvement in adsorption capacity. Comparing this sample with the others shows an increase in the adsorption capacity of an order of magnitude more.

Research revealed that a lower nanoparticle size improves its hydrogen storage efficiency. In the sample with the largest cluster, such as SPMnO-5 wt%, the uptake process was the lowest. The reason for this is probably due to a lower diffusion of hydrogen from the Pt nanoparticles to the polymeric carbon.

Different studies suggest that larger particles supply more interstitial places and, consequently, contribute to the new antibonding state formation [41,42].

The insertion of the catalyst into the composite material improves the gas sorption capacity and a kinetic benefit and evident enhancements from a thermodynamic point of view.

Considering that the temperatures in each step were not perfectly equal, varying in a range from 0.1 to 1.1 degree units, the enthalpy change ΔH and entropy change ΔS of the process were calculated following the Van 't Hoff Equation (3) below:

$$\ln p = \Delta H/RT - \Delta S/R \quad (3)$$

The corresponding straight lines of the three samples were obtained from the slopes and intercepts from where the values of $\Delta H/R$ and $\Delta S/R$ were derived. Knowing the R constant of the gases, equal to 8.31 J/mol K, the data relating to the enthalpy and entropy variation of the process were obtained. From the data shown in the inserted table in Figure 7, it can be seen that hydrogen absorption is an endothermic process for all of the samples analyzed, but when the Pt percentage increases, the enthalpy variation is significantly reduced. A similar trend can be seen when considering the entropy change, in which the sample at 10% Pt is reduced by about 95,000 J/mol·K.

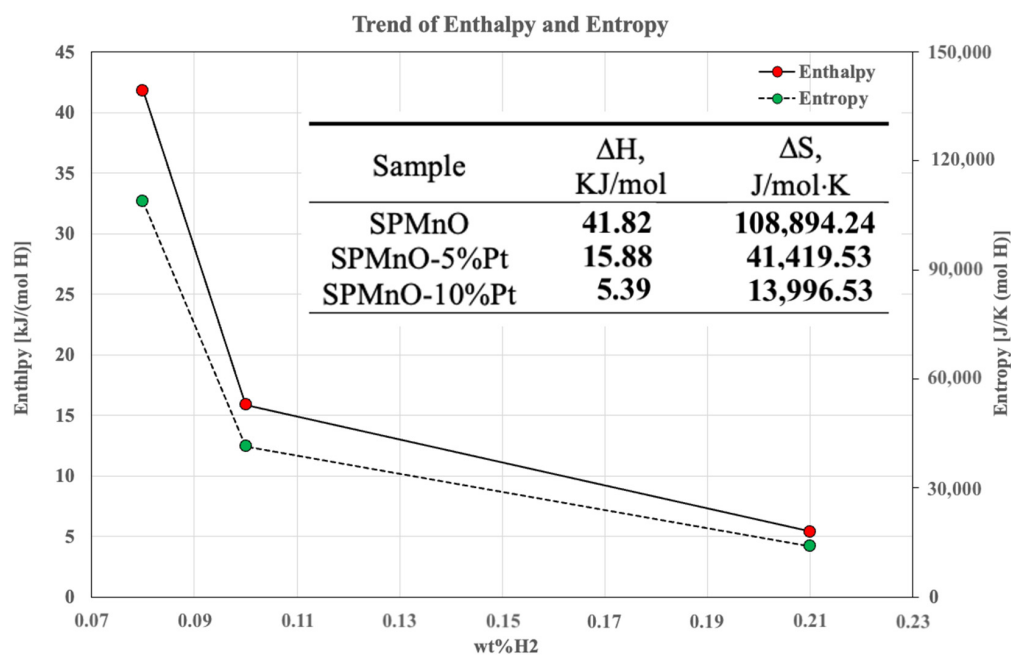


Figure 7. Enthalpy and entropy changes.

An ab initio density functional theory (DFT) modeling study was carried out considering $Mn_{22}Pt_2O_{48}$ as a supercell, as shown in Figure 8a, where the absorption of a different number of hydrogen atoms was simulated (Figure 8b–d).

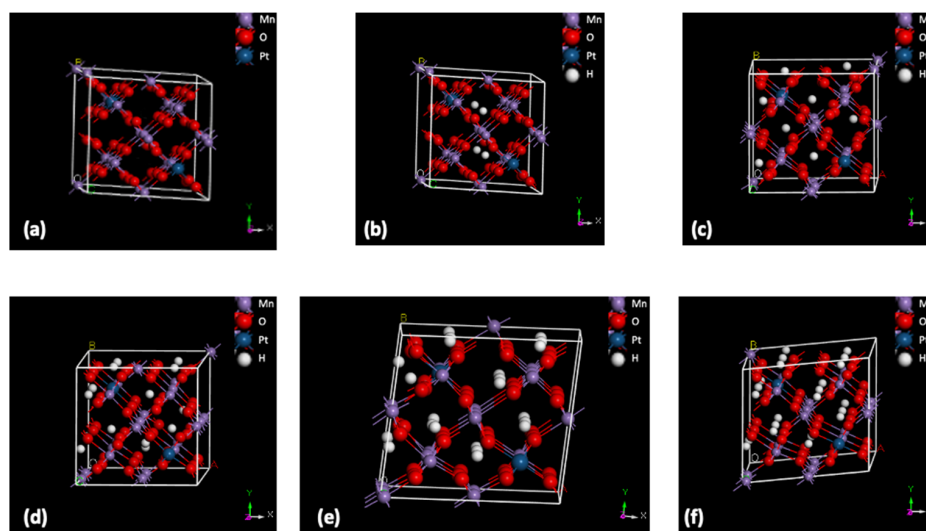


Figure 8. $Mn_{22}Pt_2O_{48}$ supercell (a); supercell containing different H_2 atoms (b–f).

In this simulation, different configurations were calculated by deriving the desorption energies of systems containing 2 to 24 hydrogen atoms located at different interstitial positions. For each energy value obtained, the corresponding theoretical hydrogen absorption percentage was derived. The relative theoretical H_2 wt% values of $Mn_{24}O_{48}H_n$ (with $n = 4, 8, 14, 22, 24$) are 0.17, 0.33, 0.59, 0.93, and 1.01, respectively. Considering the experimentally obtained results of SPMnO (0.08 wt%), SPMnO-5%Pt (0.1 wt%), and SPMnO-10%Pt (0.22 wt%), and comparing these with the theoretical data, it can be stated that the sample with a Pt load of 10% can contain approximately 5 H atoms in a supercell, which is more than twice as much as the sample with a metal load of 5% and compared to the base material.

The Desorption Energy values, obtained following Equation (1), as a function of the H atoms for $\text{Mn}_{24}\text{O}_{48}\text{H}_n$ and $\text{Mn}_{22}\text{Pt}_2\text{O}_{48}\text{H}_n$, are reported in Table 2.

Table 2. Desorption energy values with and without Pt.

H Atoms	Desorption Energy, kJ/mol	
	$\text{Mn}_{24}\text{O}_{48}\text{H}_n$	$\text{Mn}_{22}\text{Pt}_2\text{O}_{48}\text{H}_n$
2	366	301
4	296	273
6	280	273
8	271	240
10	/	221
12	234	211
14	/	214
16	/	191
18	/	184
20	/	203
22	/	207
24	175	205

The ΔE value starts from 301 kJ/mol for $n = 2$, decreases until it reaches 184 kJ/mol for $n = 18$, and then saturates to about 203–207 kJ/mol for $n = 20$ –24. Comparing the ΔE catalyzed sample value with the $\text{Mn}_{24}\text{O}_{48}$ cases, the ΔE value is lower for the $\text{Mn}_{22}\text{Pt}_2\text{O}_{48}\text{H}_n$ compared to the $\text{Mn}_{24}\text{O}_{48}\text{H}_n$ cases, with the only exception of $n = 24$. The energy desorption increases after $n = 18$ regarding $\text{Mn}_{22}\text{Pt}_2\text{O}_{48}\text{H}_n$ could be explained, as this number could represent a critical number in terms of steric encumbrance, thus inhibiting desorption processes.

As shown in Figure 9, the size of the $\text{Mn}_{22}\text{Pt}_2\text{O}_{48}$ supercell increases mainly along the y lattice constant, while the smallest variation (about 2% from $n = 0$ to $n = 24$) occurs in z. The maximum change in the lattice constant, X, occurs with the insertion of 22 hydrogen atoms, 1.4 Å, while the changes in the constants Y and Z are much smaller considering 18 H, 0.4 and 0.1 Å, respectively. In a percentage value, the lattice variations for the X, Y, and Z constants are 13%, 5%, and 1%, respectively.

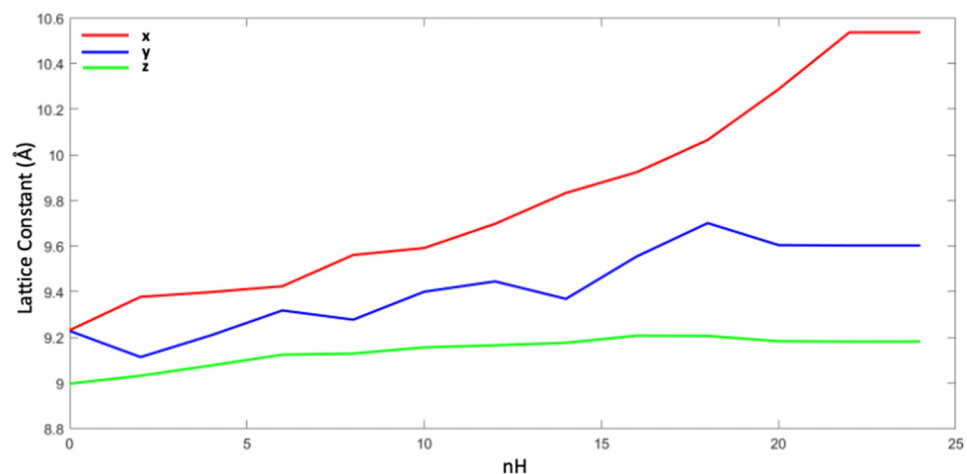


Figure 9. Changes in the lattice constants x, y, and z (blue, red, and green) of the $\text{Mn}_{22}\text{Pt}_2\text{O}_{48}\text{H}_n$ supercell.

4. Conclusions

A composite material based on manganese oxide anchored on a chlorosulphonated PEEK matrix, as previously demonstrated, shows encouraging abilities to absorb H₂, but its kinetics are quite slow. For this purpose, two percentages of metallic Pt, 5 and 10 wt%, were added to the composite material via the mechanical ball milling technique. The mixing parameters adopted, such as the sphere/powder ratio (10/1), rotation speed (300 rpm), and mixing time (3 h), were specifically selected to avoid deteriorating the polymer structure. The arrangement of Pt in the polymer matrix is more homogeneous when the metal content is 10% compared to 5%; however, some Pt agglomerates are noted, which could suggest an incomplete mixing time. This aspect was further highlighted through TEM mapping. The hydrogen absorption tests, carried out at 110 °C in a pressure range from 5 to 20 bar, showed how the addition of Pt produces multiple effects compared to the non-catalyzed material, increasing the storage capacity from 0.08 wt% to 0.2 wt%, and increasing the speed and thermodynamics of the reaction, bringing, in the latter case, the enthalpy variation from 41.82 to 5.39 KJ/mol.

Through theoretical DFT simulation studies and by considering the experimental results of hydrogen absorption, it was possible to see how the desorption energy for the catalyzed material, with nH values ranging from 2 to 12, is lower than that without Pt, starting from 301, respectively, to 211 kJ/mol, and from 366 to 234 kJ/mol. The size of the Mn₂₂Pt₂O₄₈ supercell increases mainly along the y-axis, while the smallest change occurs in the z-axis.

Author Contributions: Conceptualization, R.P. and M.S.; methodology, R.P.; software, M.S.; validation, R.P. and M.S.; formal analysis, R.P.; investigation, R.P.; resources, R.P. and M.S.; data curation, R.P. and M.S.; writing—original draft preparation, R.P.; writing—review and editing, R.P. and M.S.; visualization, R.P.; supervision, R.P.; project administration, R.P.; funding acquisition, R.P. All authors have read and agreed to the published version of the manuscript.

Funding: This research was funded by the NAUSICA (NAvi efficienti tramite l'Utilizzo di Soluzioni tecnologiche Innovative e low Carbon) project (PON "R&S 2014-2020", grant No ARS01_00334); project leader NAVTEC cluster. Total funding amount: €9,991,332.40; amount of funding per operational unit € 1,372,683.20.

Data Availability Statement: The data presented in this study are openly available in the article.

Conflicts of Interest: The funders had no role in the design of the study; in the collection, analyses, or interpretation of data; in the writing of the manuscript; or in the decision to publish the results.

References

1. Pedicini, R.; Romagnoli, M.; Santangelo, P.E. A Critical review of polymer electrolyte membrane fuel cell systems for automotive applications: Components, materials, and comparative assessment. *Energies* **2023**, *16*, 3111. [\[CrossRef\]](#)
2. Abdin, Z.; Zafaranloo, A.; Rafiee, A.; Mérida, W.; Lipinski, W.; Khalilpour, K.R. Hydrogen as an energy vector. *Renew. Sust. Energy Rev.* **2020**, *120*, 109620–109652. [\[CrossRef\]](#)
3. Carbone, A.; Gaeta, M.; Romeo, A.; Portale, G.; Pedicini, R.; Gatto, I.; Castriciano, M. Porphyrin/s-PEEK membranes with improved conductivity and durability for PEMFC technology. *ACS Appl. Energy Mater.* **2018**, *1*, 1664–1673. [\[CrossRef\]](#)
4. Gatto, I.; Saccà, A.; Carbone, A.; Pedicini, R.; Passalacqua, E. MEAs for polymer electrolyte fuel cell (PEFC) working at medium temperature. *J. Fuel Cell Sci. Technol.* **2006**, *3*, 361–365. [\[CrossRef\]](#)
5. Romagnoli, M.; Cannio, M.; Righi, S.; Santangelo, P.E.; Pedicini, R.; Carbone, A.; Gatto, I. Smart catalyst deposition by 3D printing for polymer electrolyte membrane fuel cell manufacturing. *Renew. Energy* **2021**, *163*, 414–422.
6. Wu, M.; He, J.; Xu, M.; Zhang, T.; Liu, F. Barrier identification, analysis and solutions of hydrogen energy storage application in multiple power scenarios based on improved DEMATAL-ISM approach. *Int. J. Hydrogen Energy* **2022**, *47*, 30329–30346. [\[CrossRef\]](#)
7. Marocco, P.; Gandiglio, M.; Audisio, D.; Santarelli, M. Assessment of the role of hydrogen to produce high-temperature heat in the steel industry. *J. Clean. Prod.* **2023**, *388*, 135969–135981. [\[CrossRef\]](#)
8. Tsiklios, C.; Hermesmann, M.; Müller, T.E. Hydrogen transport in large-scale transmission pipeline networks: Thermodynamic and environmental assessment of repurposed and new pipeline configurations. *Appl. Energy* **2022**, *327*, 120097–120124. [\[CrossRef\]](#)
9. Elberry, A.M.; Thakur, J.; Santasalo-Aarnio, A.; Larmi, M. Large-scale compressed hydrogen storage as part of renewable electricity storage systems. *Int. J. Hydrogen Energy* **2021**, *46*, 15671–15690. [\[CrossRef\]](#)

10. Zhang, T.; Uratani, J.; Huang, Y.; Xu, L.; Griffiths, S.; Ding, Y. Hydrogen liquefaction and storage: Recent progress and perspectives. *Renew. Sust. Energy Rev.* **2023**, *176*, 113204–113227. [CrossRef]
11. Klopčič, N.; Grimmer, I.; Winkler, F.; Sartory, M.; Trattner, A. A review on metal hydride materials for hydrogen storage. *J. Energy Storage* **2023**, *72 Pt B*, 108456–108473. [CrossRef]
12. Available online: <https://www.energy.gov/eere/fuelcells/doe-technical-targets-onboard-hydrogen-storage-light-duty-vehicles> (accessed on 30 October 2023).
13. Züttel, A. Materials for hydrogen storage. *Mater. Today* **2023**, *6*, 24–33. [CrossRef]
14. Bénard, P.; Chahine, R. Storage of hydrogen by physisorption on carbon and nanostructured materials. *Scr. Mater.* **2007**, *56*, 803–808. [CrossRef]
15. Zhang, Y.; Wu, S.; Wang, L.; Zhang, X. Chemisorption solid materials for hydrogen storage near ambient temperature: A review. *Front. Energy* **2023**, *17*, 72–101. [CrossRef]
16. Zafar, M.; Iqbal, T.; Fatima, S.; Sanuallah, Q.; Aman, S. Carbon nanotubes for production and storage of hydrogen: Challenges and development. *Chem. Pap.* **2022**, *76*, 609–625. [CrossRef]
17. Fomkin, A.; Pribylov, A.; Men'shchikov, I.; Shkolin, A.; Aksyutin, O.; Ishkov, A.; Romanov, K.; Khozina, E. Adsorption-Based hydrogen storage in activated carbons and model carbon structures. *Reactions* **2021**, *2*, 209–226. [CrossRef]
18. Pedicini, R.; Maisano, S.; Chiodo, V.; Conte, G.; Policicchio, A.; Agostino, R.G. Posidonia oceanica and wood chips activated carbon as interesting materials for Hydrogen Storage. *Int. J. Hydrogen Energy* **2020**, *45*, 14038–14047. [CrossRef]
19. Oku, T. Hydrogen storage in boron nitride and carbon nanomaterials. *Energies* **2015**, *8*, 319–337. [CrossRef]
20. Tozzini, V.; Pellegrini, V. Prospects for hydrogen storage in graphene. *Phys. Chem. Chem. Phys.* **2013**, *15*, 80–89. [CrossRef]
21. Zeleňák, V.; Saldan, I. Factors affecting hydrogen adsorption in metal-organic frameworks: A short review. *Nanomaterials* **2021**, *11*, 1638. [CrossRef]
22. Ghaffari-Tabrizi, F.; Haemisch, J.; Lindner, D. Reducing hydrogen boil-off losses during fuelling by pre-cooling cryogenic tank. *Hydrogen* **2022**, *3*, 255–269. [CrossRef]
23. Chao, B.; Klebanoff, L. Hydrogen storage technology. In *Hydrogen Storage in Interstitial Metal Hydrides*, 1st ed.; Klebanoff, L., Ed.; Taylor and Francis: Boca Raton, FL, USA, 2012; pp. 109–132.
24. Møller, K.T.; Sheppard, D.; Ravnsbæk, D.B.; Buckley, C.E.; Akiba, E.; Li, H.W.; Jensen, T.R. Complex metal hydrides for Hydrogen, thermal and electrochemical energy storage. *Energies* **2017**, *10*, 1645. [CrossRef]
25. Zhang, J.; Li, Z.; Wu, Y.; Guo, X.; Ye, J.; Yuan, B.; Wang, S.; Jiang, L. Recent advances on the thermal destabilization of Mg-based hydrogen storage materials. *RSC Adv.* **2019**, *9*, 408–428. [CrossRef] [PubMed]
26. Strozi, R.B.; Ivanisenko, J.; Koudriachova, N.; Huot, J. Effect of HPT on the first hydrogenation of LaNi₅ metal hydride. *Energies* **2021**, *14*, 6710. [CrossRef]
27. Kubo, K.; Itoh, H.; Takahashi, T.; Ebisawa, T.; Nakamura, T.; Akiba, E. Hydrogen absorbing properties and structures of Ti–Cr–Mo alloys. *J. Alloys Compd.* **2003**, *356–357*, 452–455. [CrossRef]
28. Ali, N.A.; Ismail, M. Modification of NaAlH₄ properties using catalysts for solid-state hydrogen storage: A review. *Int. J. Hydrogen Energy* **2021**, *46*, 766–782. [CrossRef]
29. Varin, R.A.; Zbroniec, L. Mechanical and thermal dehydrogenation of lithium alanate (LiAlH₄) and lithium amide (LiNH₂) hydride composites. *Crystals* **2012**, *2*, 159–175. [CrossRef]
30. Garroni, S.; Santoru, A.; Cao, H.; Dornheim, M.; Klassen, T.; Milanese, C.; Gennari, F.; Pistidda, C. Recent progress and new perspectives on metal amide and imide systems for solid-state hydrogen storage. *Energies* **2018**, *11*, 1027. [CrossRef]
31. Puzkiel, J.; Gasnier, A.; Amica, G.; Gennari, F. Tuning LiBH₄ for hydrogen storage: Destabilization, additive, and nanoconfinement approaches. *Molecules* **2020**, *25*, 163. [CrossRef]
32. Schmidt, W.R. Activity Report of the United Technologies Research Center for the Polymer Dispersed Metal Hydride Program, DOE Contract DEFC36-00G010535. Available online: <https://www.energy.gov/eere/fuelcells/articles/final-report-doe-metal-hydride-center-excellence> (accessed on 30 October 2023).
33. Liu, Z.; Lei, Z. Cyclic hydrogen storage properties of Mg milled with nickel nano-powders and MnO₂. *J. Alloys Compd.* **2007**, *443*, 121–124. [CrossRef]
34. Suttisawat, Y.; Rangsunvigit, P.; Kitiyanan, B.; Kulprathipanja, S. Effect of co-dopants on hydrogen desorption/absorption of HfCl₄- and TiO₂-doped NaAlH₄. *Int. J. Hydrogen Energy* **2008**, *33*, 6195–6200. [CrossRef]
35. Pedicini, R.; Saccà, A.; Carbone, A.; Passalacqua, E. Hydrogen storage based on the polymeric material. *Int. J. Hydrogen Energy* **2011**, *36*, 9062–9068. [CrossRef]
36. Pedicini, R.; Schiavo, B.; Rispoli, P.; Saccà, A.; Carbone, A.; Gatto, I.; Passalacqua, E. Progress in polymeric material for hydrogen storage application in middle conditions. *Energy* **2014**, *64*, 607–614. [CrossRef]
37. Pedicini, R.; Sigalas, M.; Carbone, A.; Gatto, I. Functionalised hybrid poly(ether ether ketone) containing MnO₂: Investigation of operative conditions for hydrogen sorption. *Int. J. Hydrogen Energy* **2017**, *42*, 10089–10098. [CrossRef]
38. Pedicini, R.; Matera, F.; Giacompo, G.; Gatto, I.; Passalacqua, E. Performance assessment of an integrated PEFC and an hydrogen storage device based on innovative material. *Int. J. Hydrogen Energy* **2015**, *40*, 17388–17393. [CrossRef]
39. Shah, M.A. Growth of uniform nanoparticles of platinum by an economical approach at relatively low temperature. *Sci. Iran.* **2012**, *19*, 964–966. [CrossRef]

40. Sun, Y.; Zhuang, L.; Lu, J.; Hong, X.; Liu, P. Collapse in crystalline structure and decline in catalytic activity of Pt nanoparticles on reducing particle size to 1 nm. *J. Am. Chem. Soc.* **2007**, *129*, 15465–15467. [[CrossRef](#)]
41. Zhong, M.; Fu, Z.; Yuan, L.; Zhao, H.; Zhu, J.; He, Y.; Wang, C.; Tang, Y. A solution-phase synthesis method to prepare Pd-doped carbon aerogels for hydrogen storage. *RSC Adv.* **2015**, *5*, 20966–20971. [[CrossRef](#)]
42. Zubizarreta, L.; Menéndez, J.A.; Pis, J.J.; Arenillas, A. Improving hydrogen storage in Ni-doped carbon nanospheres. *Int. J. Hydrogen Energy* **2009**, *34*, 3070–3076. [[CrossRef](#)]

Disclaimer/Publisher’s Note: The statements, opinions and data contained in all publications are solely those of the individual author(s) and contributor(s) and not of MDPI and/or the editor(s). MDPI and/or the editor(s) disclaim responsibility for any injury to people or property resulting from any ideas, methods, instructions or products referred to in the content.